Geophysical Journal International

Geophys. J. Int. (2013) doi: 10.1093/gji/ggt141

Geophysical Journal International Advance Access published April 23, 2013

Inversion for coseismic slip distribution of the 2010 M_w 6.9 Yushu Earthquake from InSAR data using angular dislocations

Guoyan Jiang,[1,2] Caijun Xu,[1,2] Yangmao Wen,[1,2] Yang Liu,[1,2] Zhi Yin[1,2] and Jianjun Wang[1,2]

[1] *School of Geodesy and Geomatics, Wuhan University,* 129 *Luoyu Road, Wuhan,* 430079*, China. E-mail: cjxu@sgg.whu.edu.cn*

[2] *Key Laboratory of Geospace Environment and Geodesy, Ministry of Education, Wuhan University,* 129 *Luoyu Road, Wuhan,* 430079*, China*

Accepted 2013 April 8. Received 2013 April 5; in original form 2012 March 10

SUMMARY

We used interferometric SAR (InSAR) crustal deformation data sets to explore the fault slip involved in the 2010 April 14 ($M_w = 6.9$) Yushu earthquake modelled using angular dislocations. A refined rupture trace of the Yushu fault was extracted from two InSAR coseismic interferograms and field investigation results. We present a new method to discretize the fault geometry using triangular dislocation elements (TDEs), which are able to maintain consistency with the fault geometry modelled using rectangular dislocation elements (RDEs) and to avoid dislocation gaps and overlaps. Comprehensive comparisons between RDE and TDE models indicate that the classic Laplacian operator, which has not been carefully explored in many published studies, minimizes the slip on the boundary RDEs of the fault. A modification is proposed for the development of reasonable RDE models. The inversion shows that there were two larger concentrated slip zones during the Yushu earthquake. The largest was southeast of the hypocentre, near Luorongda, with a maximum slip of ∼1.6 m at the surface. The smaller slip patch was in the middle of the fault at a depth of ∼6 km, near the hypocentre. To improve the computational efficiency, we re-derived the analytic expressions for the strains associated with angular dislocations in an elastic half-space. The Coulomb stress changes increase at the northwestern and southeastern ends of the fault, and the small number of aftershocks in the southeast indicates that the seismic risk may be elevated in this area.

Key words: Inverse theory; Radar interferometry; Earthquake ground motions; Dynamics and mechanics of faulting; Asia.

1 INTRODUCTION

On 2010 April 13 (UTC 23:49:37), an M_w 6.9 earthquake struck Yushu, Qinghai, China, causing the death of more than 2200 people and damaging over 80 per cent of the buildings in the area (Zhang *et al*. 2010). The hypocentre of the main shock was located at 33.2°N, 96.6°E at a depth of 14 km. The largest aftershock was located at 33.23°N, 96.58°E at a depth of 10 km. Both earthquakes occurred on the left-lateral Ganzi-Yushu fault, which strikes WNW–ESE. The Ganzi-Yushu fault is approximately 500 km long and is located at the southern border of the Bayankara block and at the northern border of the Qiangtang block. It is in the northwestern part of the Xianshuihe-Xiaojiang fault system (Fig. 1), which includes the Ganzi-Yushu, Xianshuihe, Anninghe, Zemuhe, Daliangshan and Xiaojiang faults. This fault system bounds the northern edge of the southeastern block of the Tibetan Plateau (Zhang *et al*. 2005; He *et al*. 2006).

Based on field investigations (Chen *et al*. 2010; Lin *et al*. 2011; Guo *et al*. 2012), the primary ground rupture zone lies between Luorongda and Sangka Counties on the northwestern part of the Ganzi-Yushu fault, with a total length ranging from 31 to 33 km (Fig. 1). In the south of the Longbao pull-apart lake, there is an ∼8.5-km-long surface rupture and a 2-km-long en-echelon tension fracture. The maximum horizontal displacement is 1.8 m at 33°04′22.5″N, 96°49′31.9″E, approximately 16 km from Yushu. Several studies have estimated the slip distribution for the M_w 6.75∼6.9 Yushu earthquake based on interferometric SAR (InSAR) observations or *P* waveforms (Table 1; Zhang *et al*. 2010; Li *et al*. 2011; Shan *et al*. 2011; Tobita *et al*. 2011; Zha *et al*. 2011; Wen *et al*. 2013), with maximum modelled slips of 1.32–2.6 m.

We examined the differences in the slip models for the Yushu earthquake that result from the use of mesh dislocation elements. We compared inversions using triangular dislocation elements (TDEs) to those using rectangular dislocation elements (RDEs), which are more commonly used, and we carefully examined the smoothing operators used with both types of dislocation element. The use of TDEs stems from angular dislocations in an elastic whole-space, which was first proposed by Yoffe (1960). Comninou & Dundurs (1975) derived analytic solutions for displacements in a half-space, and Jeyakumaran *et al*. (1992) constructed the stress and

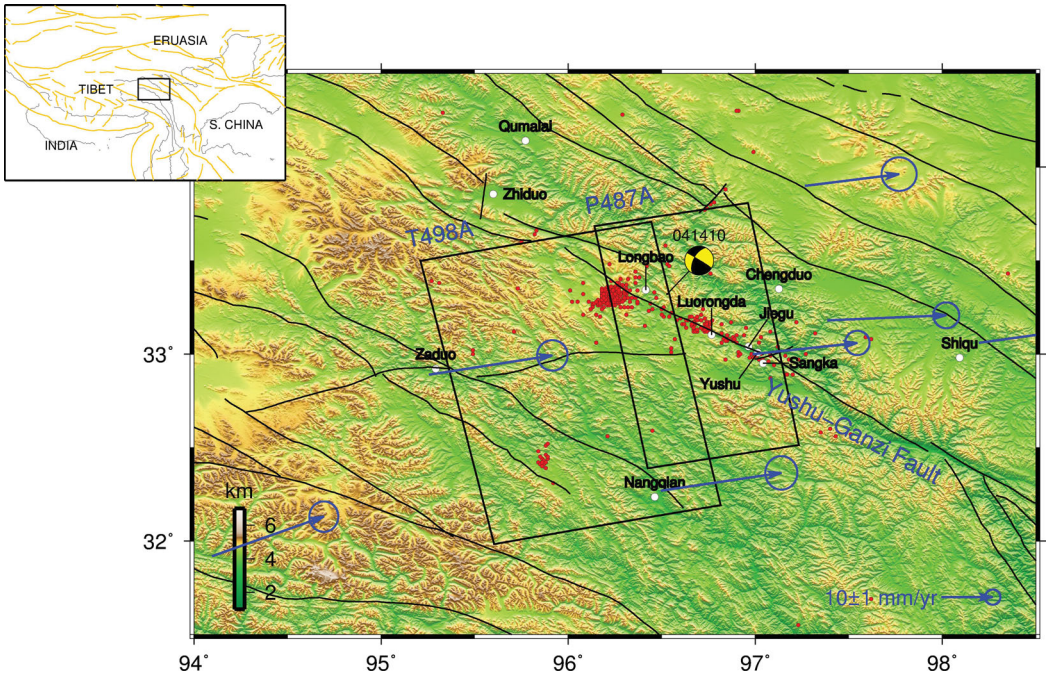

Figure 1. Topographic and tectonic map of the region surrounding the 2010 Yushu earthquake. The blue arrows show the interseismic GPS velocities before the Yushu earthquake relative to a stable Eurasia with 95 per cent confidence ellipses (2σ; Gan *et al*. 2007). The black–yellow beach ball is the focal mechanism of the earthquake as taken from the GCMT project (http://www.globalcmt.org). The red circles show the $M \geq 2.0$ aftershocks.

Table 1. The fault models, observations and partial inversion results from published studies and this study.

Sources		Segments	Total length (km)	Width (km)	Dip (°)	Dislocation element	Size (km)	Max. slip (m)	M_w	Data
Zhang *et al*. (2010)		1	96	30	83	RDE	3 × 3	1.8	6.90	*P* waves
Tobita *et al*. (2011)		8	76	10	90	RDE	2 × 2	∼2.6	6.78	ALOS PALSAR T487A[a] ALOS PALSAR T139D[a]
Li *et al*. (2011)		3	80	20	70∼90	RDE	1 × 1	1.5	6.83	ENVISAT ASAR T498A ALOS PALSAR T487A
Shan *et al*. (2011)		1	–	22	85	RDE	3 × 3	∼1.5	–	ALOS PALSAR T487A
Zha *et al*. (2011)		4	66.25	20∼25	82∼86	RDE	1 × 1	1.32	6.75	ALOS PALSAR T487A
Wen *et al*. (2013)		4	86.1	20	67∼100	RDE	∼2 × 2	2.0	6.90	ALOS PALSAR T487A ALOS PALSAR T139D[a]
This study	Model A	12	96.72	25	90	RDE	1.4 × 1.4	1.78	6.82	
	Model B	12	96.72	25	83	RDE	1.4 × 1.4	1.81	6.80	
	Model C	12	96.72	25	90	TDE	1 × 2	1.39	6.78	ENVISAT ASAR T498A
	Model D	12	96.72	25	81	TDE	∼1 × 2[b]	1.64	6.81	ALOS PALSAR T487A
	Model E[c]	12	96.72	25	90	RDE	1.4 × 1.4	1.43	6.76	
	Model F[c]	12	96.72	25	83	RDE	1.4 × 1.4	1.61	6.76	

[a]The ALOS PALSAR P139D data were acquired from the descending path in ScanSAR mode.
[b]The sizes of TDEs are not equal, as a result of the spline interpolation while discretizing the fault surface.
[c]The inversions for the slip models were carried out using the modified Laplacian operator.

displacement fields for a TDE in a half-space by superposing the angular dislocations. This solution has been implemented in the boundary element code Poly3D (Thomas 1993), which has been expanded to Poly3Dinv to invert for slip (Resor 2003). Meade (2007) defined a triangle vertex ordering scheme to calculate the deformation fields from multiple TDEs. Many studies (e.g. Resor 2003; Bürgmann *et al*. 2005; Maerten *et al*. 2005; Resor *et al*. 2005; Schmidt *et al*. 2005; Murray & Langbein 2006; Zhang *et al*. 2008; Belabbès *et al*. 2009; Furuya & Yasuda 2011; Loveless & Meade 2011; Miyazaki *et al*. 2011; Ochi & Kato 2011) have applied TDEs to explore seismic and aseismic fault slip. The advantage of utilizing TDEs is that complex fault geometries can be modelled without dislocation gaps or overlaps.

In this study, we defined an improved ground rupture trace of the main fault active in the Yushu earthquake using the line-of-sight (LOS) coseismic deformation field (Fig. 2). A new method for constructing the fault geometry with TDEs by using the fault parameters (e.g. width, length, depth, strike and dip) was developed to maintain consistency with the fault surface represented with RDEs. We discretized multiplanar vertical or dipping faults using both TDEs and RDEs for further slip inversions. Comprehensive comparisons between RDE and TDE models were carried out to explore the following three questions. (1) Are the RDE and TDE slip models identical for a vertical fault? If not, why? (2) What will be the influences of the dislocation gaps and overlaps for a non-vertical fault? (3) For the Yushu earthquake, which type of slip model is more appropriate?

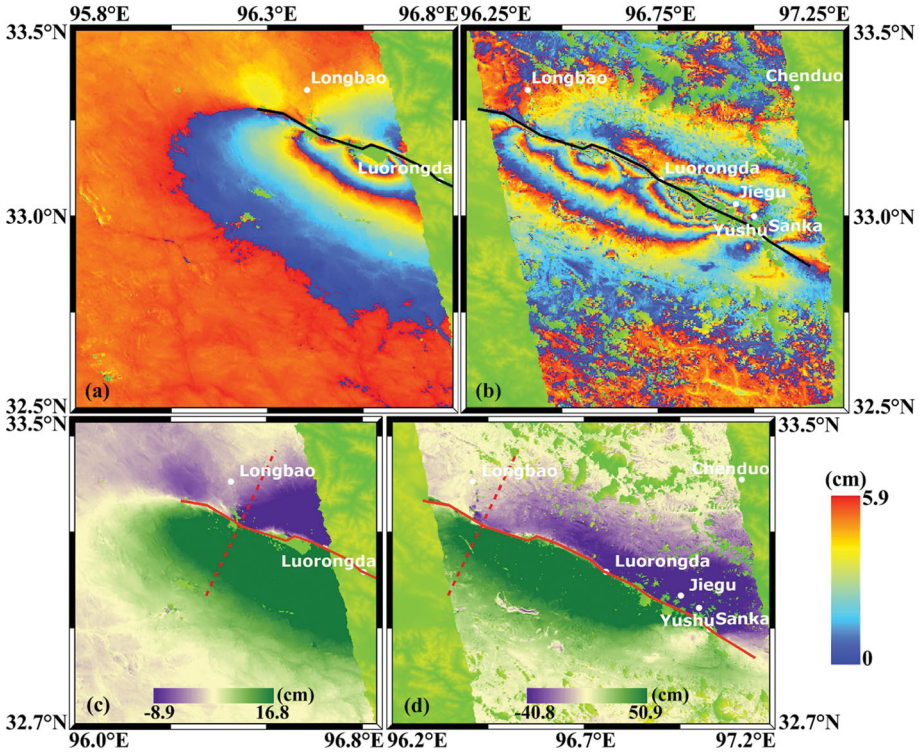

Figure 2. Interferograms and the extracted ground rupture trace of the Yushu earthquake. The positive sign indicates a lengthening of the range between the surface and the satellite. Panels (a) and (c) show the interference fringe pattern and the deformation field, respectively, from a pair of ENVISAT ASAR images. Panels (b) and (d) show the interference fringe pattern and deformation field, respectively, from a pair of ALOS PALSAR images. The two deformation fields, (c) and (d), are rendered with contrasting colours to highlight the position of the displacement jumps (red solid line). The red dashed line is the dividing line used in extracting the rupture trace.

2 InSAR-BASED COSEISMIC DEFORMATION AND FAULT GEOMETRY

2.1 InSAR-based coseismic deformation

A pair of ALOS Phased Array type L-band Synthetic Aperture Radar (PALSAR) images and a pair of ENVISAT Advanced Synthetic Aperture Radar (ASAR) images (Table 2) were used to obtain the coseismic deformation field using the Caltech/JPL software ROI_PAC (version 3.1 beta; Rosen *et al*. 2004) in two-pass differential interferometry mode. The topographic phase was removed using the Shuttle Radar Topography Mission (SRTM) three arc-second (∼90 m) digital elevation model (DEM). The interferograms were corrected for differences in satellite position using precise orbits from the ESA and JAXA. The interferograms were then unwrapped using the SNAPHU programmme (Chen & Zebker 2000) and geocoded to a geographic coordinate system.

The nearly symmetrical deformation field is 82 km long and 40 km wide and is centred on the Yushu fault (Fig. 2). The elliptical fringes in Fig. 2(b) demonstrate that larger changes in LOS occurred in two places, with the largest one near the southeastern portion of the fault. On the south side of the fault, the displacements to the west are greater than those to the east. In contrast, on the north side of the fault, the LOS changes are greater to the east than those to the west. This deformation pattern suggests that the fault slip is mainly left-lateral.

Table 2. Basic parameters of the two interferograms.

Satellite	Master	Slave	$B_\perp$ (m)	T (days)	Track
ALOS	100 115	100 417	712	92	487
ENVISAT	100 215	100 426	8	72	498

2.2 Fault geometry

The coseismic deformation field (Figs 2c and d) on the north and south sides of the fault has displacement jumps due to the movement of the hangingwall relative to the footwall. There is a 24-km-long gap in the surface rupture between Longbao and Luorongda Counties (Guo *et al*. 2012), where we assume that the fault rupture remained near the surface. Thus, the location of the steep displacement gradient can be considered to be the ground rupture trace of the fault. The segments to the northwest of the dashed red line (Fig. 2c) were extracted based on the coseismic deformation field obtained from a pair of ENVISAT ASAR images. The segments to the southeast of this line were extracted based on the coseismic deformation field obtained from a pair of ALOS PALSAR images (Fig. 2d). The fault was separated into 12 segments from the northwest to the southeast; the parameters describing these segments are shown in Table 3. Based on the inversion of InSAR observations from Shan *et al*. (2011), Li *et al*. (2011), Tobita *et al*. (2011), Zha *et al*. (2011) and Wen *et al*. (2013), there is negligible slip on the Yushu fault surface below a depth of 25 km, which is the fault width considered in our slip inversions.

Using the parameters in Table 3, we discretized the multiplanar vertical and dipping faults with both TDEs and RDEs. When the dipping multiplanar fault surface with RDEs is modelled, dislocation gaps and overlaps become apparent, which is a common phenomenon (Li *et al*. 2011; Zha *et al*. 2011). These undesirable

Table 3. Parameters for each fault segment indexed from northwest to southeast.

Segment #	Longitude (°)	Latitude (°)	Length (km)	Strike (°)	Width (km)
1	96.28	33.29	6.612	101.606	25
2	96.35	33.28	11.111	125.626	25
3	96.45	33.22	11.191	111.119	25
4	96.56	33.19	2.466	58.875	25
5	96.58	33.20	4.848	112.443	25
6	96.63	33.18	9.992	120.228	25
7	96.72	33.14	4.672	136.308	25
8	96.76	33.11	8.554	118.939	25
9	96.84	33.07	5.202	130.450	25
10	96.88	33.04	13.078	118.208	25
11	97.00	32.98	6.193	134.445	25
12	97.05	32.94	12.797	126.011	25

dislocation gaps and overlaps may negatively influence the resulting slip models (e.g. Maerten *et al*. 2005), and they can induce high-magnitude strain and stress concentrations at their edges, as demonstrated by Meade (2007). Some studies (e.g. Zweck *et al*. 2002) have presented methods to minimize these gaps or overlaps, but constructing a fault surface with no dislocation gaps or overlaps is necessary.

The use of TDEs is a good solution for this problem. In this study, we have developed a new method to discretize the fault surface using TDEs based upon the modelling procedure of RDEs. We expected the fault surface constructed with TDEs to be consistent with the geometry of the RDE model, allowing for a comprehensive comparison between the RDE and TDE models. Taking a multiplanar dipping fault with three segments (Fig. 3; Table 4) as an example, we first modelled each fault segment using uniformly sized RDEs based on the parameters of the segments (node coordinates, widths and dips). Fig. 3(a) shows the fault surface discretized with RDEs. The resulting dislocation overlaps and gaps are delineated by the dotted red lines. The gridpoints (corners of the RDEs) located in the overlapping area should be removed. Then, we interpolated the remaining gridpoints in each row using a spline to maintain a consistent number of gridpoints and smooth the overlaps and gaps between adjacent segments with different strikes, which increase with depth. This step yields a fault surface without dislocation gaps or overlaps patched with the quadrangular dislocation elements (QDEs) rather

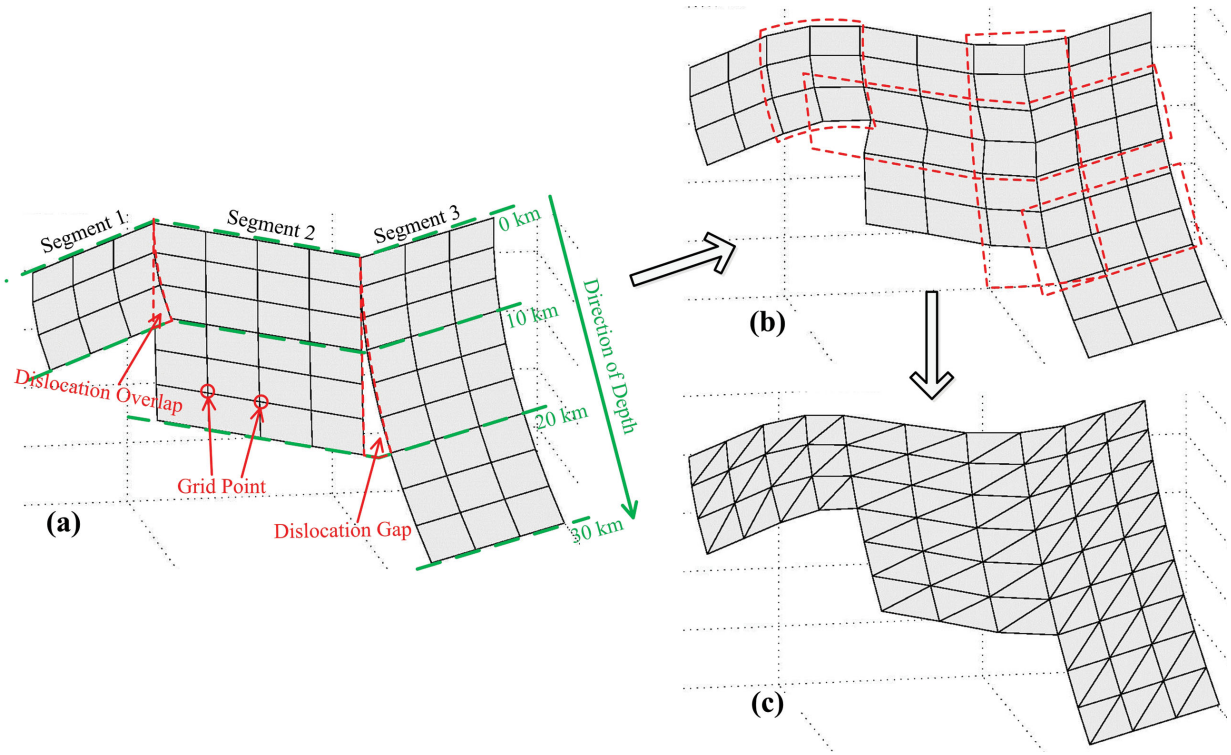

Figure 3. An illustration of the method of modelling the fault geometry with TDEs. Along the strike, there are three segments with widths of 10, 20 and 30 km. (a) The fault surface is patched with RDEs, where the dislocation overlap and gap arise, obtained from the first step. (b) The fault surface patched with QDEs obtained after the first spline interpolation. (c) The final fault surface patched with TDEs.

Table 4. The statistical results for six slip models using the same observations.

Model	Moment (N m)	Misfit (cm)	Ratio[a]	*F* test	Per cent[b]
A	2.09×10^{19}	1.17	0.7750		76 per cent
B	1.97×10^{19}	1.14	0.8163	Significance Level: 0.01	72 per cent
C	1.81×10^{19}	1.08	0.9096	Degrees of freedom: 3665	75 per cent
D	2.04×10^{19}	1.03	–	Refused domain: >1.0559	75 per cent
E	1.71×10^{19}	1.14	0.8163		76 per cent
F	1.71×10^{19}	1.11	0.8611		70 per cent

[a]The misfit of Model D is taken as the numerator.
[b]The statistical results of aftershocks located in the regions of increased Coulomb failure stress.

than RDEs (Fig. 3b). However, interpolation can cause changes in the dip of QDEs, which are more obvious in the columns and rows within the dotted red polygons. Therefore, further spline interpolation for the QDE gridpoints in each column was necessary to smooth the dips of the QDEs in these zones. Fig. 3(c) shows the final fault geometry discretized using QDEs. Dividing each QDE diagonally produces the TDEs.

Triangular irregular networks (TIN) are the most commonly used method of constructing triangles of a given curved fault surface (e.g. Maerten *et al*. 2005; Meade 2007; Furuya & Yasuda 2011). However, the construction procedure is cumbersome, as described by Ochi & Kato (2011), which may be one reason why TDE is not as popular as RDE (Maerten *et al*. 2005). Many types of software, such as Poly3D, GOCAD and MATLAB, have been introduced to discretize the curved fault surface. Compared to the TIN method, our method can more easily control the dip and strike of the curved fault surface at arbitrary positions by assigning specific RDEs. Using this method, we discretized the geometry of the Yushu fault into ∼1 km (strike length) × 2 km (vertical width) TDEs, which is consistent with the fault geometry modelled with 1.4 × 1.4 km RDEs.

3 INVERSION FOR THE SLIP DISTRIBUTION

The two interferograms provide more than 10^6 observations that are highly correlated in space (Fig. 2). To reduce the spatial correlation and the number of observations involved in the inversion and to improve the computational efficiency, the interferograms were compressed using the quadtree algorithm proposed by Welstead (1999). Jónsson *et al*. (2002) introduced this algorithm into InSAR inversions, and Lohman & Simons (2005) discussed it in further detail. In this study, the maximum sampling window was 64 × 64 pixels, and the minimum was 8 × 8 pixels. The threshold value of the root mean square (rms) was set to 0.4 cm for the ALOS PALSAR interferogram and 0.3 cm for the ENVISAT ASAR interferogram. A total of 3666 observations were obtained from the ALOS PALSAR interferogram, 0.16 per cent of the original number, and 786 observations were obtained from the ENVISAT ASAR interferogram, 0.02 per cent of the original group.

Using the 4452 down-sampled InSAR observations, the amount of slip on each TDE was inverted using the bounded variable least-squares (BVLS) algorithm (Stark & Parker 1995), which is based on the elastic half-space angular dislocation model (Comninou & Dundurs 1975). To avoid singularities in the slip distribution, the scale-dependent umbrella smoothing operator ∇^2 (Desbrun *et al*. 1999; Maerten *et al*. 2005) was added into the inversion. The function model used in the inversion process can be formulated as follows:

$$\begin{bmatrix} \boldsymbol{d}' \\ \boldsymbol{0} \end{bmatrix} = \begin{bmatrix} \boldsymbol{G}' & \boldsymbol{L} \\ k^2\nabla^2 & \boldsymbol{0} \end{bmatrix} \begin{bmatrix} \boldsymbol{m} \\ \boldsymbol{s} \end{bmatrix}, \quad \boldsymbol{d}' = \boldsymbol{U}d, \quad \boldsymbol{G}' = \boldsymbol{U}G, \quad \boldsymbol{W} = \boldsymbol{U}^{\mathrm{T}}\boldsymbol{U},$$

$$\boldsymbol{L} = \begin{bmatrix} \boldsymbol{\Delta}x^1 & \boldsymbol{\Delta}y^1 & \boldsymbol{1} & \boldsymbol{0} & \boldsymbol{0} & \boldsymbol{0} \\ \boldsymbol{0} & \boldsymbol{0} & \boldsymbol{0} & \boldsymbol{\Delta}x^2 & \boldsymbol{\Delta}y^2 & \boldsymbol{1} \end{bmatrix},$$

$$\boldsymbol{s} = \begin{bmatrix} s_1^1 & s_2^1 & s_0^1 & s_1^2 & s_2^2 & s_0^2 \end{bmatrix}^T, \tag{1}$$

where $\boldsymbol{d}$ is the vector containing observations, $\boldsymbol{m}$ is the slip vector, $\boldsymbol{G}$ is Green's function matrix, $\boldsymbol{W}$ is the weight matrix for the observations and $\boldsymbol{U}$ is the upper triangular matrix from the Cholesky decomposition of $\boldsymbol{W}$. An overall linear offset $\boldsymbol{L}s$ may exist between the InSAR observations and the model result $\boldsymbol{G}'m$, which is primarily attributed to the residual orbit error. Taking the centre point $(\boldsymbol{\lambda}_0^i,\ \varphi_0^i)$ of the ith interferogram as a reference, $\boldsymbol{\Delta}x^i = R\cos\boldsymbol{\varphi}^i(\boldsymbol{\lambda}^i - \lambda_0^i; i = 1, 2)$ denotes the east–west distances of the observations related to the reference, and $\boldsymbol{\Delta}y^i = R(\boldsymbol{\varphi}^i - \varphi_0^i)$ denotes the north–south distances. R is radius of the Earth. s_0^i is the overall offset of the InSAR observations. s_1^i and s_2^i are the deformation gradients in the east–west and north–south directions, respectively. The multiplier k^2 before the umbrella operator ∇^2 determines the smoothness.

The roughness of the slip distribution can be calculated using

$$\rho = \frac{\sum_{i=1}^{2n} |p_i|}{2n}, \qquad \boldsymbol{p} = \nabla^2 m, \tag{2}$$

where n is the number of dislocation elements. The weighted misfit of the InSAR observations to the sum of the model results and the overall linear offset is expressed by

$$\boldsymbol{\Phi} = \boldsymbol{V}^{\mathrm{T}}V, \quad \boldsymbol{V} = \boldsymbol{d}' - \boldsymbol{G}'m - \boldsymbol{L}t. \tag{3}$$

The roughness ρ decreases with k, whereas the weighted misfit Φ simultaneously increases. The trade-off curve between the weighted misfit and roughness requires k to balance these variables.

We developed two types of fault model: multiplanar vertical and dipping fault models, which are discretized with both RDEs and TDEs. The multiplanar vertical and dipping RDE slip models are referred to as Model A and B, respectively, and the multiplanar vertical and dipping TDE slip models are referred to as Model C and D, respectively. When implementing the inversion for RDE slip models, we adopted the model described above. Green's function matrix $\boldsymbol{G}$ was built using the Okada (1992) elastic half-space dislocation model. The slip solutions were smoothed by minimizing the second-order derivative (Laplacian) of the fault slip in addition to the residual norm (Jónsson *et al*. 2002). A smoothing factor $k^2 = 0.3$ was selected from the trade-off curves (Fig. 4) for the inversions when the fault dips were fixed at 90°. The optimal dips of the multiplanar and dipping fault models were determined according to the relationship between the weighted residual sum of squares and the dips (Fig. 5) with the selected smoothing factor. Four coseismic slip models for the 2010 Yushu earthquake (Figs 6a–d) were obtained from the inversion using the function models and the selected smoothing factor.

4 DISCUSSION

4.1 Comparison between the RDE and TDE slip models

The four slip models in Figs 6(a–d) all have two concentrated slip zones. The spatial patterns of slip in the RDE and TDE slip models vary little for the two dip angles. The maximum slips in the vertical and dipping RDE models (Figs 6a and b) are 1.78 and 1.81 m, respectively, and they occur at similar locations at approximately 6 km depth. However, the maximum slips in the two TDE models are 1.39 and 1.64 m, respectively, and are located at the ground surface near Luorongda. This phenomenon also appears in the modelled slip distributions of the 1999 October 16 M_w 7.1 Hector Mine earthquake in southern California (RDE slip distribution in fig. 8 of Jónsson *et al*. 2002; TDE slip distribution in fig. 5 of Maerten *et al*. 2005).

The fault geometries shown in Figs 6(a) and (c) are the same, and the sizes of the RDEs and TDEs used to discretize them were designed to be similar (i.e. 1.96 and 2 km^2, respectively). The

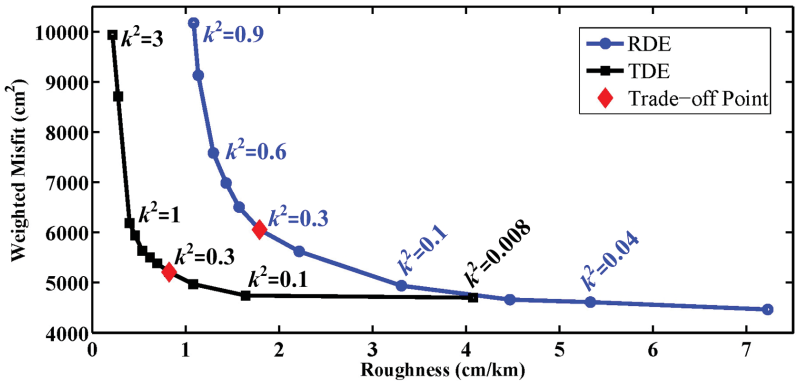

Figure 4. Trade-off curves between the weighted misfit and the roughness. The dip of the fault is assumed to be 90°. The blue and black lines show the results from the inversions for the slip distributions on RDEs and TDEs, respectively. The preferred smoothing factor ($k^2 = 0.3$) is indicated by the red diamonds.

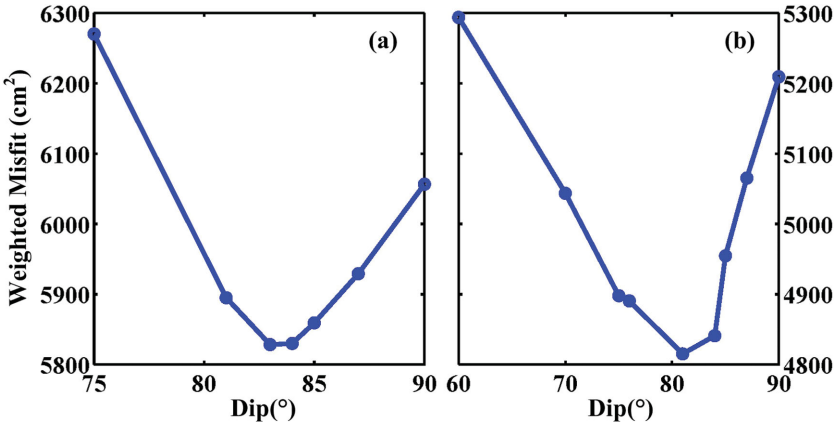

Figure 5. The weighted residual sum of squares for different dips of the Yushu fault. (a) For the RDE slip models, an optimal dip of 83° is chosen. (b) For the TDE slip models, an optimal dip of 81° is chosen.

same smoothing factor was used in the inversion to minimize the influence of the different discretization of the slip distribution (e.g. Zhang *et al.* 2011). Consequently, the discrepancy in the size and location of maximum slip is probably due to the different smoothing operators used in the inversions. When we went back to check these two smoothing operators, it was found that the Laplacian operator (Jónsson *et al.* 2002) used in the RDE case implicitly minimized the slip on the boundary RDEs along the fault. The formula of the Laplacian operator is written as

$$\frac{S_{i,j-1} - 2S_{i,j} + S_{i,j+1}}{(\Delta l_R)^2} + \frac{S_{i-1,j} - 2S_{i,j} + S_{i+1,j}}{(\Delta l_C)^2}, \tag{4}$$

where $S_{i,j}$ is the slip on the patch in the ith row and jth column of the fault and Δl_R and Δl_C are the distances between adjacent patches in the row and column directions, respectively. Generally, there are four adjacent patches for an RDE, but there are only three adjacent patches for the boundary RDEs and two for the RDEs at each of the four corners of the fault. For these corner RDEs, doubling the slip in the numerators of eq. (4) means that the slip must be halved to obtain the expected smoothness between two adjacent RDEs, which is obviously unreasonable.

For further comparison, we modified the classical Laplacian smoothing operator for the boundary RDEs. For the corner RDEs, the operator was replaced with

$$\frac{S_{i,c} - S_{i,j}}{(\Delta l_R)^2} + \frac{S_{r,j} - S_{i,j}}{(\Delta l_C)^2}, \tag{5}$$

where $S_{i,c}$ and $S_{r,j}$ are the slip on the adjacent patches in the direction of row and column, respectively. c is equal to $j-1$ or $j+1$, and r is equal to $i-1$ or $i+1$. For the RDEs in the top and bottom rows of the fault, the operator was replaced with

$$\frac{S_{i,j-1} - 2S_{i,j} + 2S_{i,j+1}}{(\Delta l_R)^2} + \frac{S_{r,j} - S_{i,j}}{(\Delta l_C)^2}, \tag{6}$$

where r is equal to $i-1$ or $i+1$. For the boundary RDEs in the columns, the operator was replaced with

$$\frac{S_{i,c} - S_{i,j}}{(\Delta l_R)^2} + \frac{S_{i-1,j} - 2S_{i,j} + S_{i+1,j}}{(\Delta l_C)^2}, \tag{7}$$

where c is equal to $j-1$ or $j+1$.

Using the modified Laplacian smoothing operator, the two RDE slip models were updated with the same smoothing value used in the above inversions. Fig. 6(e) (Model E) and 6(f) (Model F) are the vertical and dipping RDE models, respectively. Their maximum slip values are 1.43 and 1.61 m, respectively, which is very similar to the two TDE models (Models C and D), both of which have the maximum slip near the ground surface. The multiplanar vertical and dipping fault geometries discretized with RDEs and TDEs have a good consistency.

The six modelled seismic moments are listed in Table 4, using an elastic shear modulus μ of 3.2×10^{10} Pa. Table 1 presents the corresponding magnitudes of this event. The predicted InSAR interferograms from these six models and the residual fringes are documented in Figs 7 and 8, respectively. The rms misfits between the InSAR observations and the predicted LOS displacements from

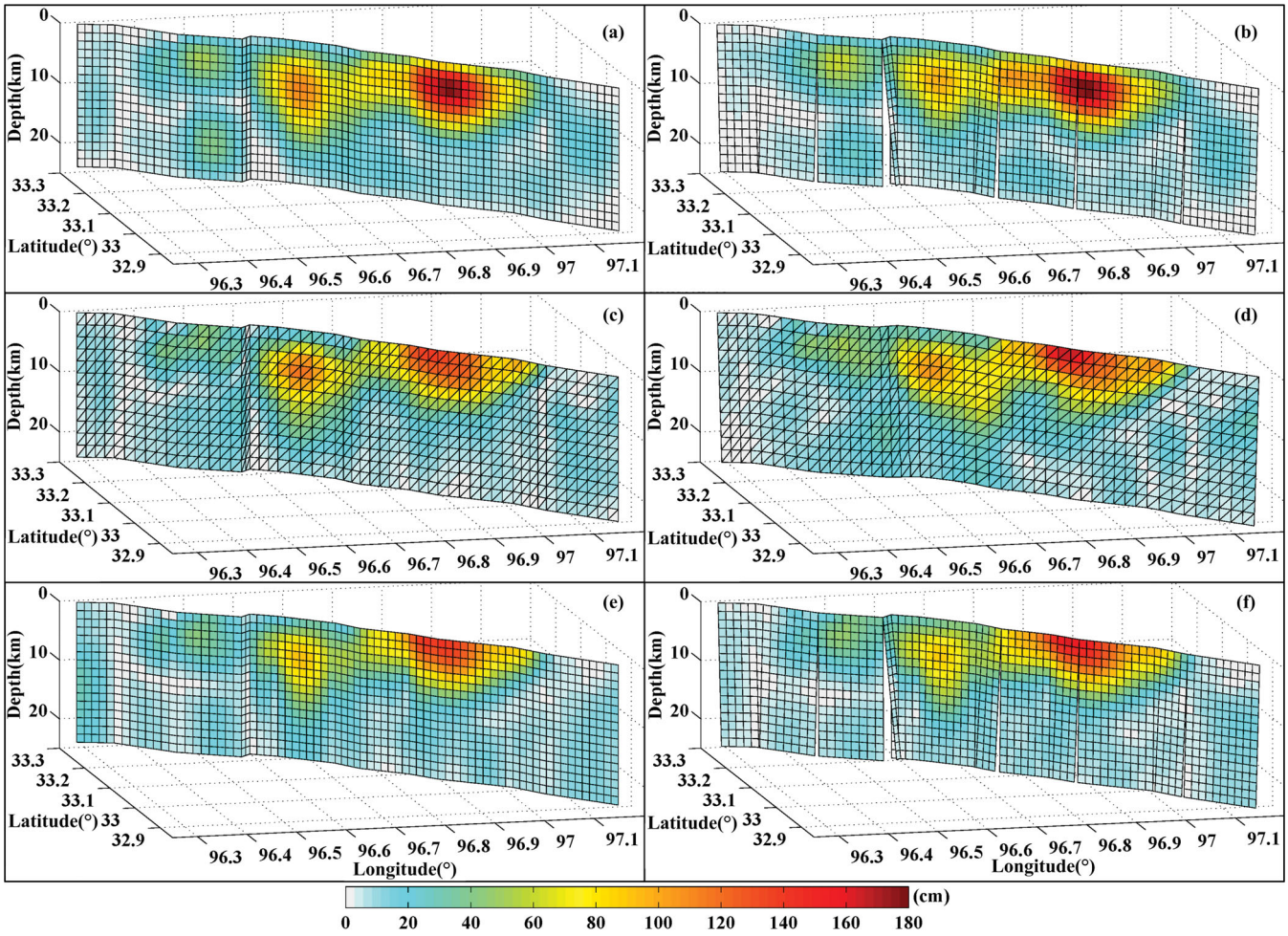

Figure 6. Fault geometries modelled with RDEs and TDEs and slip distributions inferred from the InSAR displacements. A smoothing value of 0.3 was used in these inversions. The dips of the faults in the left column are 90°, the dips of the faults in panels (b) and (f) are 83° and the dip of the fault in panel (d) is 81°. The slip models in panels (a) and (b) (Models A and B, respectively) were obtained from the inversion using the classical Laplacian operator. The slip models in panels (e) and (f) (Model E and F, respectively) were obtained from the inversion using the modified Laplacian operator. The maximum slip values in panels (a), (b), (c), (d), (e) and (f) are 1.78, 1.81, 1.39, 1.64, 1.43 and 1.61 m, respectively.

these six slip models range from 1.03 to 1.17 cm (Table 4). Using the TDE models rather than the RDE models with the classic Laplacian smoothing operator results in an approximately 10 per cent improvement in the rms misfit. The updated RDE models decrease the misfits to the InSAR observations compared to the two earlier RDE models. The fit to the InSAR observations of the TDE Model C increases by ∼5 per cent compared with the modified RDE Model E. The fit of the TDE Model D increases by ∼7 per cent, which is superior to the modified RDE Model F.

We carried out an F test to test the hypothesis that the misfit variance of the TDE Model D is lower than that of the other five models. The significance level was set to 0.01. None of the ratios of the variance of Model D to the five other models is larger than $F_{0.01}(3665, 3665;$ equal to 1.0559; Table 4), which means the confidence level of this hypothesis is 99 per cent. Consequently, the above misfit comparison results are reliable.

4.2 Comparison with other slip models

In addition to our slip distributions, several slip models of the Yushu earthquake have been published using different observations (Table 1). Zhang *et al*. (2010) and Shan *et al*. (2011) modelled the source fault as a single dipping fault, Li *et al*. (2011) divided the fault into three dipping segments, Tobita *et al*. (2011) divided the fault into eight vertical segments and Zha *et al*. (2011) and Wen *et al*. (2013) used four dipping subfaults.

The slip model given by Zhang *et al*. (2010) shows two larger concentrated slip zones (their Fig. 3). The largest patch of slip is located in the southeast of the hypocentre near Luorongda, with a maximum slip of 1.8 m near the surface. A similar pattern can be observed in the models of Shan *et al*. (2011), Li *et al*. (2011) and Wen *et al*. (2013). The maximum slips in Shan *et al*. (2011) (their Fig. 2d) and Wen *et al*. (2013) (their Fig. 6b) are approximately 2.0 m and are near the ground surface. The positions of the largest slip in the models of Zhang *et al*. (2010) and Shan *et al*. (2011), both of which use a single-planar fault, are similar to our TDE models and updated RDE models.

Li *et al*. (2011) first inverted *P* and *SH* waveforms to solve for the parameters of three fault segments and then modelled the slip distribution on 1 × 1 km RDEs using the same InSAR observations as in this study as well as additional ENVISAT ASAR T004D data. The maximum slip in their model is ∼1.5 m and occurs at a depth of ∼4 km (their Fig. 7). Their results show that the distributed slip

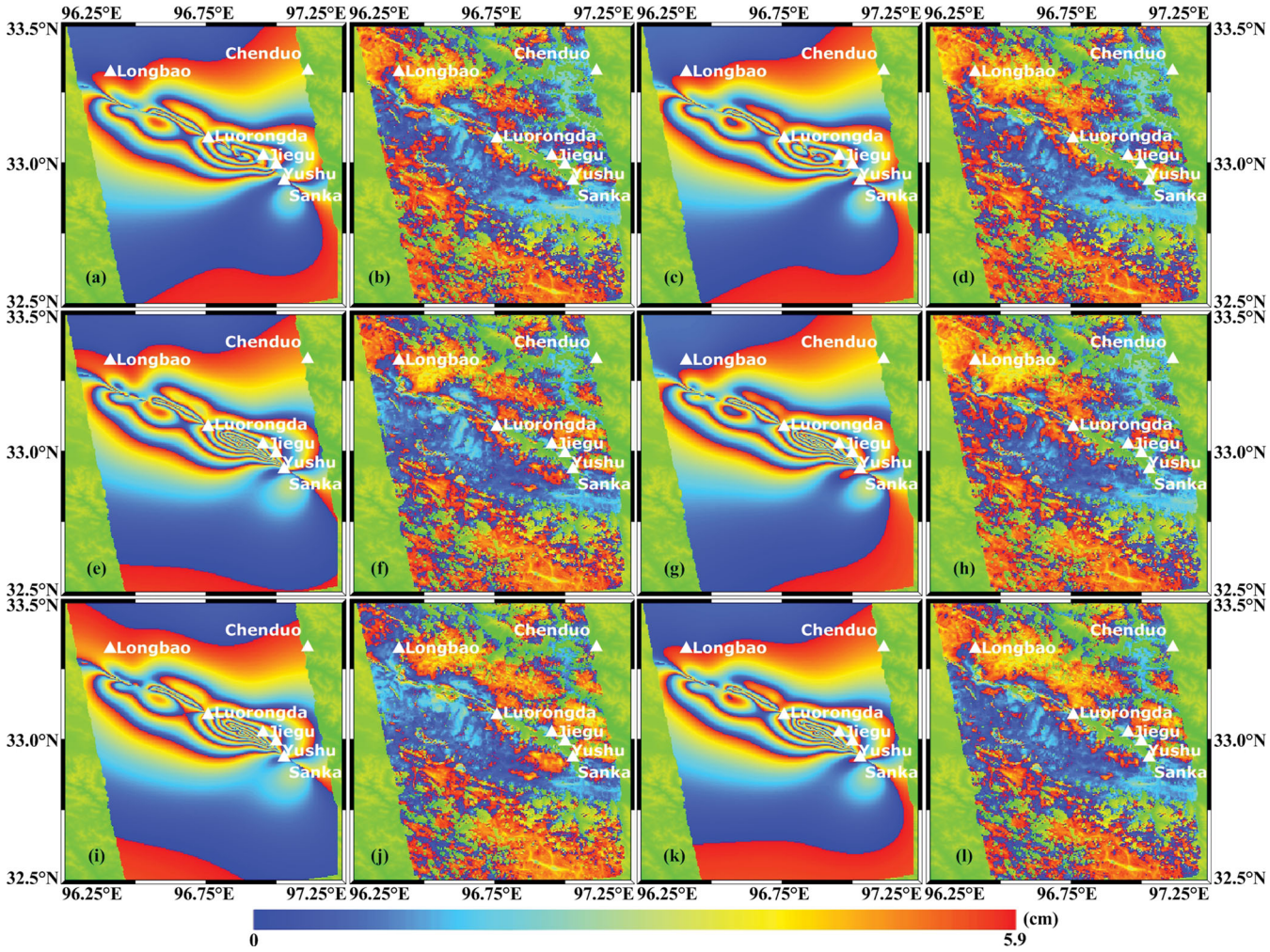

Figure 7. The modelled interferograms and residual fringes for the ALOS PALSAR T487 observations. Panels (a), (c), (e), (g), (i) and (k) show the predicted interference fringe patterns for the slip models in Fig. 6, in sequence. Panels (b), (d), (f), (h), (j) and (l) show the residual fringes between the InSAR data and the models.

model released a seismic moment of 2.2×10^{19} N m, and the rms misfit to the ALOS T487A interferograms is 1.6 cm. The slip model of Li *et al*. (2011) is similar to the results of Wen *et al*. (2013) (their Fig. 3) and our Model B using the classic Laplacian operator. The largest slip described by Wen *et al*. (2013) is located between the depths of 2 and 4 km. The maximum slip of 1.81 m in Model B (Fig. 6b) occurred at a depth of 2.8∼4.2 km near Luorongda. The released seismic moment is 1.81×10^{19} N m, and the rms misfit of our model with InSAR observations is 1.14 cm.

The slip model obtained by Zha *et al*. (2011) revealed three main slip patches (their Fig. 5). The positions of the largest and the second largest slip patches are similar to the four published slip models described above. The third largest patch of slip is located southeast of the city of Yushu, with a maximum slip of approximately 0.9 m, which is unique to this model. The slip model of Tobita *et al*. (2011) shows the largest differences in the magnitude and position of the maximum slip (their Fig. 6a) of the five published slip models described here. The largest slip patch is in the middle of the fault near the hypocentre at a depth of 4∼8 km, with a maximum slip of ∼2.6 m. Although the cause of the differences is ambiguous, the use of a vertical fault and eight fault segments (the largest number of any published study) by Tobita *et al*. (2011) can be excluded as the cause. The slip models in Fig. 6 show that dip has some influence on the magnitude of the largest slip but not the position. Up to 12 fault segments are used in our models, and the six models maintain a good consistency with the published models described above. The difference in the depths of maximum slip indicates that the smoothing operators used in the published inversions may not have been carefully inspected.

Compared to the predicted InSAR interferograms and residual fringes given by Shan *et al*. (2011), Li *et al*. (2011), Zha *et al*. (2011) and Wen *et al*. (2013), our six models improve the fit to the InSAR observations. There are no residual fringes in the near field along the surface projection of the fault segments in our Figs 7 and 8, unlike these four published studies, which is mainly a result of the complex rupture trace extracted in our study. From this perspective, our models are more accurate than these published slip models.

4.3 Static coulomb stress change

Jeyakumaran *et al*. (1992) outlined the expressions for calculating the stress field associated with angular dislocations, and Meade (2007) differentiated the Green's functions given by Comninou & Dundurs (1975) with symbolic algebra software. However, it remains difficult to account for the stress induced by the slip at each angular dislocation. A set of analytical expressions, shown

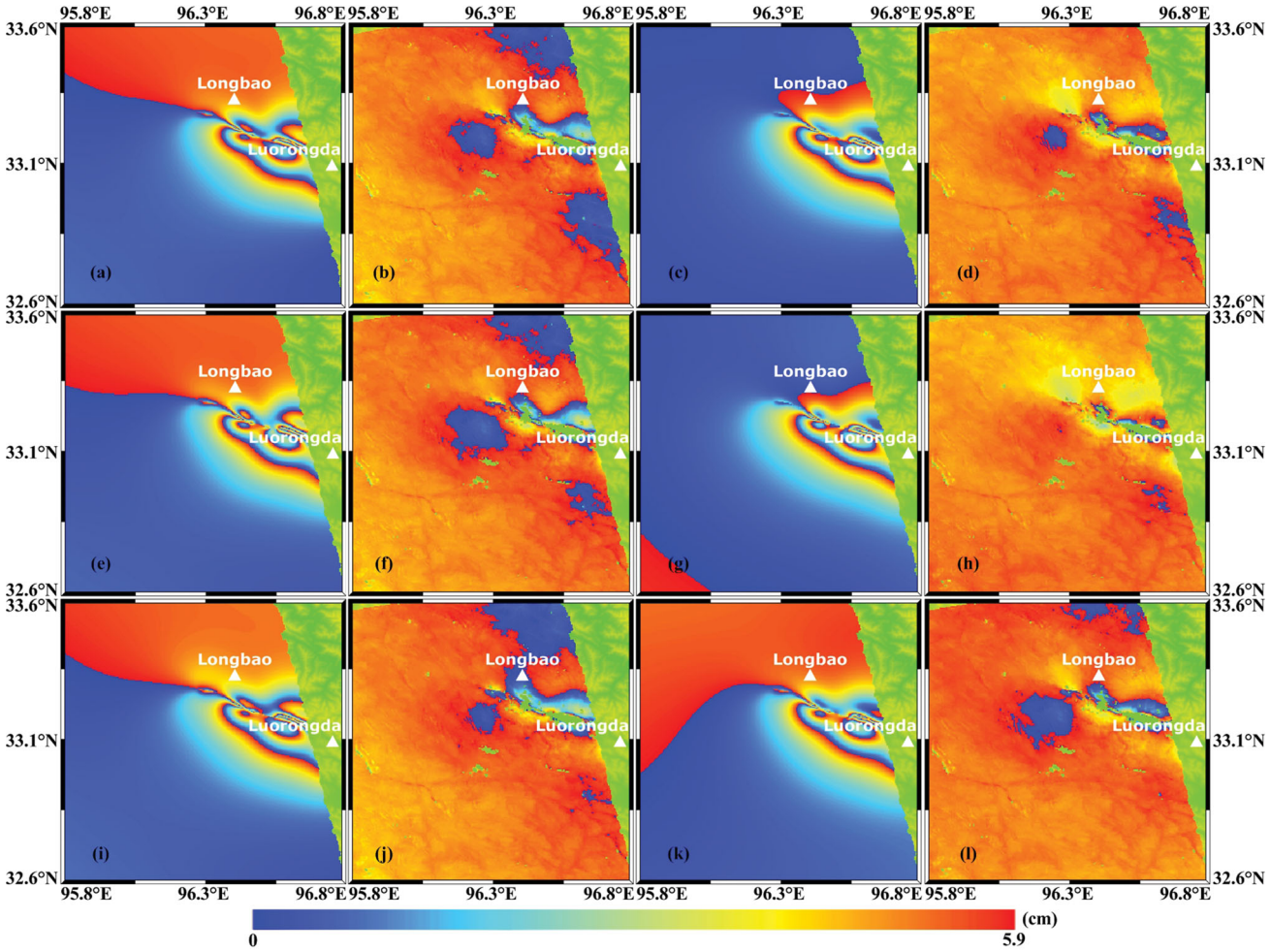

Figure 8. The modelled interferograms and residual fringes for the ENVISAT ASAR T498 observations. Panels (a), (c), (e), (g), (i) and (k) show the predicted interference fringe patterns for the slip models in Fig. 6, in sequence. Panels (b), (d), (f), (h), (j) and (l) show the residual fringes between the InSAR data and the models.

in the auxiliary materials, for calculating the strains in an elastic half-space from the angular dislocations was derived and programed in an M-file and C# language. The terms frequently used in the formulae were extracted to improve the computational efficiency. We ran the two codes on the same PC as a comparison (Appendix A), which showed that our code is ∼13 times faster than the version given in Meade (2007).

Using these strain formulae, the coseismic static Coulomb stress change (Fig. 9) on optimally orientated 2-D fault planes (King *et al*. 1994) at a depth of 10 km triggered by the Yushu earthquake was predicted using the six slip models (Fig. 6). The regional principal compressive stress was set to 100 bars and oriented to N70°E based on the 2008 release of the World Stress Map (Heidbach *et al*. 2010). The effective coefficient of friction was assumed to 0.2 based on the strike-slip motion along the Yushu fault.

The results revealed that the stresses increased at both the northwestern and southeastern ends of the Yushu fault, which is consistent with the results of Shan *et al*. (2011) and Wen *et al*. (2013). Fig. 9 shows $M \geq 2.0$ aftershocks from 2010 April 14 to 2011 December 16, as obtained from the International Seismological Centre (ISC) bulletin. Aftershocks are concentrated in the northwest of the Yushu fault, but there are few aftershocks in the southeast. The seismic risk may be elevated in the southeast due to the lower stress release. Statistical results (Table 4) show that the aftershocks were concentrated in the regions of increased Coulomb failure stress induced by the six slip models (Fig. 6). Among these models, the RDE slip models with dislocation gaps and overlaps exhibit the lowest percentage.

5 CONCLUSION

Our new method developed to model fault geometries using TDEs maintains close consistency with the fault geometry represented with RDEs and avoids dislocation gaps and overlaps. The comparison of Models A–F reveals that the classic Laplacian smoothing operator minimizes the slip on the boundary RDEs of the fault, which is the primary reason for differences between RDE Model A and TDE Model C, as these two models differ only in the type of dislocation element and corresponding smoothing operator. The different depths of maximum slip in six published models suggest that the smoothing operators used in many inversions are not examined carefully.

The TDE models improve the fit to the InSAR observations by 5∼10 per cent compared to the four RDE models. The misfits of two updated RDE models are less than the RDE Models A and B. Compared with published studies, our six slip models produce the lowest misfit, which is mainly due to the refined ground rupture trace. Based on this comparison, we conclude that the TDE

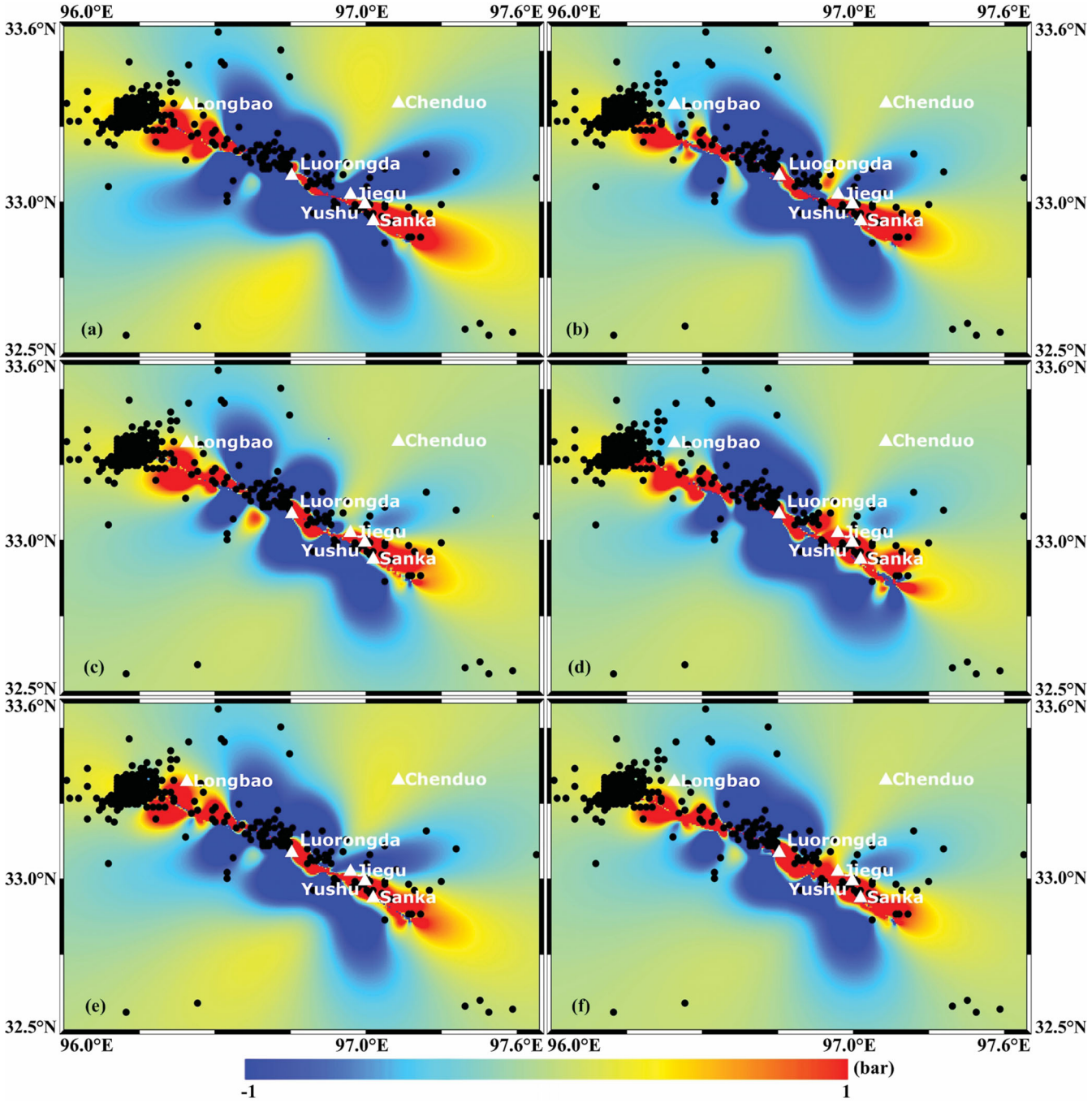

Figure 9. Coseismic changes in static Coulomb stresses triggered by the Yushu earthquake and its aftershocks (black circles). The regional tectonic stress was set to 10 MPa oriented N70°E. The order of the slip models used here is the same as in Fig. 6.

Model D is the most reasonable model and that TDEs are a good choice for slip inversion involving complex rupture traces. Model D shows that there are two larger concentrated slip zones involved in the M_w 6.81 Yushu earthquake. The largest modelled slip is southeast of the hypocentre, near Luorongda, with up to 1.64 m of slip at the surface. The second largest slip patch is in the middle of the fault near the hypocentre.

The analytical strain expressions derived in this study increase the computing efficiency by a factor of ∼13 compared to the code presented by Meade (2007). This difference is mainly attributable to the extraction of terms that are frequently used. The changes in the calculated static Coulomb stress show that Coulomb stresses increased at the northwestern and southeastern ends of the fault. The seismic risk may be elevated in the southeast because of accumulated stress that was not sufficiently released by sparse aftershocks.

ACKNOWLEDGEMENTS

We thank Editor Duncan Agnew, Prof. Jeffrey Freymueller and an anonymous reviewer for their thoughtful reviews, which lead to substantial improvements to this paper. This work is cosupported by the State Key Development Program for Basic Research of China (No. 2013CB733300), the National Department Public Benefit Research Foundation (Earthquake) (No. 201308009),

the National Natural Science Foundation of China (No. 41074007, 41021061, 41204010 and 41204043), the Doctoral Fund of Ministry of Education of China (No. 20110141130010, 20100141120033 and 20090141110055), the Fundamental Research Funds for the Central Universities (No. 3101036 and 114035) and the Open Research Fund Program of the Key Laboratory of Geospace Environment and Geodesy, Ministry of Education, China (11–02–05). All ENVISAT SAR data are copyrighted by the European Space Agency and provided under CAT-1 project (ID: 7195). We also acknowledge JAXA gratefully for providing ALOS SAR data (RA3 608). The aftershocks data are obtained from ISC at http://www.isc.ac.uk/iscbulletin/search/bulletin/. Fig. 1 is plotted using the Generic Mapping Tools (version 4.5.1; www.soest.hawaii.edu/gmt; Wessel & Smith 1998). Figs 3, 4 5 and 6 are made using the MATLAB (version 2010b).

REFERENCES

Belabbès, S., Wicks, C., Çakir, Z. & Meghraoui, M., 2009. Rupture parameters of the 2003 Zemmouri (M_w 6.8), Algeria, earthquake from joint inversion of interferometric synthetic aperture radar, coastal uplift, and GPS, *J. geophys. Res.,* **114,** B03406, doi:10.1029/2008JB005912.

Bürgmann, R., Kogan, M.G., Steblov, G.M., Hilley, G., Levin, V.E. & Apel, E., 2005. Interseismic coupling and asperity distribution along the Kamchatka subduction zone, *J. geophys. Res.,* **110,** B07405, doi:10.1029/2005JB003648.

Chen, C.W. & Zebker, H.A., 2000. Network approaches to two-dimensional phase unwrapping: intractability and two new algorithms, *J. Opt. Soc. Am. A. Opt. Image Sci. Vis.,* **17,** 401–414.

Chen, L.C. *et al.*, 2010. The M_s7.1 Yushu earthquake surface rupture and large historical earthquakes on the Garzê-Yushu Fault, *Chin. Sci. Bull.,* **55**(31), 3504–3509 (in Chinese).

Comninou, M. & Dundurs, J., 1975. The angular dislocation in a half space, *J. Elasticity,* **5,** 203–216.

Desbrun, M., Meyer, M., Schroder, P. & Barr, A.H., 1999. Implicit fairing of irregular meshes using diffusion and curvature flow, *SIGGRAPH,* **99,** 317–324.

Furuya, M. & Yasuda, T., 2011. The 2008 Yutian normal faulting earthquake (M_w 7.1), NW Tibet: non-planar fault modelling and implications for the Karakax Fault, *Tectonophysics,* **511**(3), 125–133.

Gan, W., Zhang, P., Shen, Z.-K., Niu, Z., Wang, M., Wan, Y., Zhou, D. & Cheng, J., 2007. Present-day crustal motion within the Tibetan Plateau inferred from GPS measurements, *J. geophys. Res.,* **112,** B08416, doi:10.1029/2005JB004120.

Guo, J.M., Zheng, J.J., Guan, B.B., Fu, B.H., Shi, P.L., Du, J.G., Xie, C. & Liu, L., 2012. Coseismic surface rupture structures associated with 2010 M_s 7.1 Yushu earthquake, China, *Seis. Res. Lett.,* **83,** 109–118.

He, H.L., Ran, H.L. & Ikada, Y., 2006. Uniform strike-slip rate along the Xianshuihe-Xiaojiang fault system and its implications for active tectonics in southeastern Tibet, *Acta Geol. Sin.,* **2,** 376–386.

Heidbach, O., Tingay, M., Barth, A., Reinecker, J., Kurfeß, D. & Müller, B., 2010. Global crustal stress pattern based on the World Stress Map database release 2008, *Tectonophysics,* **482,** 3–15.

Jeyakumaran, M., Rudnicki, J.W. & Keer, L.M., 1992. Modeling slip zones with triangular dislocation elements, *Bull. seism. Soc. Am.,* **82,** 2153–2169.

Jónsson, S., Zebker, H., Segall, P. & Amelung, F., 2002. Fault slip distribution of the 1999 M_w 7.1 Hector Mine, California, earthquake, estimated from satellite radar and GPS measurements, *Bull. seism. Soc. Am.,* **92,** 1377–1389.

King, G.C.P., Stein, R.S. & Lin, J., 1994. Static stress changes and the triggering of earthquakes, *Bull. seism. Soc. Am.,* **84,** 935–953.

Li, Z., Elliott, J.R., Feng, W., Jackson, J.A., Parsons, B.E. & Walters, R.J., 2011. The 2010 M_w 6.8 Yushu (Qinghai, China) earthquake: constraints provided by InSAR and body wave seismology, *J. geophys. Res.,* **116,** 10 302–10 318.

Lin, A.M., Rao, G., Jia, D., Wu, X.J., Yan, B. & Ren, Z.K., 2011. Co-seismic strike-slip surface rupture and displacement produced by the 2010 M_w 6.9 Yushu earthquake, China, and implications for Tibetan tectonics, *J. Geodyn.,* **52,** 249–259.

Lohman, R.B. & Simons, M., 2005. Some thoughts on the use of InSAR data to constrain models of surface deformation, *Geochem. Geophys. Geosyst.,* **6**(1), Q01007, doi:10.1029/2004GC000841.

Loveless, J.P. & Meade, B.J., 2011. Spatial correlation of interseismic coupling and coseismic rupture extent of the 2011 M_w = 9.0 Tohoku-oki earthquake, *Geophys. Res. Lett.,* **38,** L17306, doi:10.1029/2011GL048561.

Maerten, F., Resor, P., Pollard, D. & Maerten, L., 2005. Inverting for slip on three-dimensional fault surfaces using angular dislocations, *Bull. seism. Soc. Am.,* **95,** 1654–1665.

Meade, B.J., 2007. Algorithms for the calculation of exact displacements, strains, and stresses for triangular dislocation elements in a uniform elastic half space, *Comp. Geosci.,* **33**(8), 1064–1075.

Miyazaki, S., McGuire, J.J. & Segall, P., 2011. Seismic and aseismic fault slip before and during the 2011 off the Pacific coast of Tohoku Earthquake, *Earth Planets Space,* **63,** 637–642.

Murray, J. & Langbein, J., 2006. Slip on the San Andreas Fault at Parkfield, California, over two earthquake cycles, and the implications for seismic hazard, *Bull. seism. Soc. Am.,* **96**(4B), S283–S303.

Ochi, T. & Kato, T., 2011. The plate coupling in the Tokai District, the Central Japan, inferred from the different data using triangular dislocation elements, *Tectonophysics,* **497**(1–4), 15–22.

Okada, Y., 1992. Internal deformation due to shear and tensile faults in a half-space, *Bull. seism. Soc. Am.,* **82,** 1018–1040.

Resor, P.G., 2003. Deformation associated with continental normal faults, *PhD thesis,* Stanford University, USA.

Resor, P.G., Pollard, D.D., Wright, T.J. & Beroza, G.C., 2005. Integrating high-precision aftershock locations and geodetic observations to model coseismic deformation associated with the 1995 Kozani-Grevena earthquake, Greece, *J. geophys. Res.,* **110,** B09402, doi:10.1029/2004JB003263.

Rosen, P.A., Hensley, S., Peltzer, G. & Simons, M., 2004. Updated Repeat Orbit Interferometry package released, *EOS, Trans. Am. geophys. Un.,* **85**(5), 47.

Schmidt, D.A., Bürgmann, R., Nadeau, R.M. & d'Alessio, M., 2005. Distribution of aseismic slip rate on the Hayward fault inferred from seismic and geodetic data, *J. geophys. Res.,* **110,** B08406, doi:10.1029/2004JB003397.

Shan, B., Xiong, X., Zheng, Y., Wei, S.J., Wen, Y.M., Jin, B.K. & Ge, C., 2011. The co-seismic Coulomb stress change and expected seismicity rate caused by 14 April 2010 M_s = 7.1 Yushu, China, earthquake, *Tectonophysics,* **510**(3–4), 345–353.

Stark, P.B. & Parker, R.L., 1995. Bounded variable least squares: an algorithm and application, *J. Comp. Stat.,* **10,** 129–141.

Thomas, A.L., 1993. Poly3D: a three-dimensional, polygonal element, displacement discontinuity boundary element computer program with applications to fractures, faults, and cavities in the earth's crust, *MS thesis,* Stanford University, USA.

Tobita, M., Nishimura, T., Kobaysahi, T., Hao, K.X. & Shindo, Y., 2011. Estimation of coseismic deformation and a fault model of the 2010 Yushu earthquake using PALSAR interferometry data, *Earth planet. Sci. Lett.,* **307,** 430–438.

Welstead, S.T., 1999. *Fractal and Wavelet Image Compression Techniques,* pp. 51–54, SPIE Optical Engineering Press, Bellingham, Washington.

Wen, Y., Xu, C., Liu, Y., Jiang, G. & He, P., 2013. Coseismic slip in the 2010 Yushu earthquake (China), constrained by wide-swath and strip-map InSAR, *Nat. Hazards Earth Syst. Sci.,* **13,** 35–44.

Wessel, P. & Smith, W.H.F., 1998. New, improved version of Generic Mapping Tools released, *EOS, Trans. Am. geophys. Un.,* **79**(47), 579.

Yoffe, E.H., 1960. The angular dislocation, *Phil. Mag.,* **5**(50), 161–175.

Zha, X.J., Dai, Z.Y., Ge, L.L., Zhang, K., Li, X.J., Chen, X.F., Li, Z.H. & Fu, R.S., 2011. Fault geometry and slip distribution of the 2010 Yushu earthquakes inferred from InSAR measurement, *Bull. seism. Soc. Am.,* **101**(4), 1951–1958.

Zhang, G.H., Qu, C.Y., Shan, X.J., Song, X.G., Zhang, G.F., Wang, C.S., Hu, J.C. & Wang, R.J., 2011. Slip distribution of the 2008 Wenchuan M_S 7.9 earthquake by joint inversion from GPS and InSAR measurements: a resolution test study, *Geophys. J. Int.,* **186,** 207–220.

Zhang, G.M., Ma, H.S., Wang, H. & Wang, X.L., 2005. Boundaries between active-tectonic blocks and strong earthquakes in the China mainland, *Chin. J. Geophys.,* **48**(3), 602–610 (in Chinese).

Zhang, L., Wu, J.C., Ge, L.L., Ding, X.L. & Chen, Y.L., 2008. Determining fault slip distribution of the Chi-Chi Taiwan earthquake with GPS and InSAR data using triangular dislocation elements, *J. Geodyn.,* **45,** 163–168.

Zhang, Y., Xu, L.S. & Chen, Y.T., 2010. Source process of the 2010 Yushu, Qinghai, earthquake, *Sci. China Earth Sci.,* **40**(7), 819–821 (in Chinese).

Zweck, C., Freymueller, J.T. & Cohen, S.C., 2002. Elastic dislocation modeling of the postseismic response to the 1964 Alaska earthquake, *J. geophys. Res.,* **107,** B42064, doi:10.1029/2001JB000409.

APPENDIX A. COMPARISON OF THE CODE OF MEADE (2007) AND THAT RE-PROGRAMMED IN THIS STUDY TO CALCULATE THE STRAINS DUE TO ANGULAR DISLOCATIONS

We rewrote the 'Strains due to the Angular Dislocations' code in a MATLAB file to provide a fair comparison with the code given in Meade (2007). The strains at 280 × 320 locations, the number of which is equal to the number of points in Fig. 9 due to the slip on a TDE, were calculated using these two codes. The calculation was implemented in the same computing environment (CPU: Intel(R) Core(TM) 2 6300 @ 1.86 GHz, Memory: 3.00 GB, OS: Windows 7 x86, MATLAB version 2010b). The strains obtained from these two codes are equal to within 1E-16. The run time for Meade's code is 177.661604 s, and the run time for our code is 13.225929 s; this difference is mainly due to the extraction of frequently used terms in the formulae.

The data used for comparison are included in the supplement. The file 'data for comparison.mat' contains the matrixes (*X*s, *Y*s and *Z*s) giving the station coordinates; the matrixes (Tri_x, Tri_y and Tri_z) giving the TDE coordinates; the variables (U1, U2 and U3) giving the strike, dip and tensile slip displacements, respectively; and the two structs (Strain1 and Strain2) giving the strains obtained from Meade's code and our code, respectively.

SUPPORTING INFORMATION

Additional Supporting Information may be found in the online version of this article:

Appendix S1. Six slip models (Model A-F) and their format specifications.
Appendix S2. The strain expressions associated with the angular dislocation in an elastic half-space.
Appendix S3. The codes for calculating the strains due to Burgers vector on an Angular Dislocation Element written in an M-file and C# language respectively.
Appendix S4. Data for comparison between the Meade's code and our Matlab code (http://gji.oxfordjournals.org/lookup/suppl/doi:10.1093/gji/ggt141/-/DC1)

Please note: Oxford University Press are not responsible for the content or functionality of any supporting materials supplied by the authors. Any queries (other than missing material) should be directed to the corresponding author for the article.